Ore Geology Reviews 142 (2022) 104704

Contents lists available at ScienceDirect

Ore Geology Reviews

journal homepage: www.elsevier.com/locate/oregeorev

Metallogenic potential of the Wulong goldfield, Liaodong Peninsula, China revealed by high-resolution ambient noise tomography

Fan Zheng [a,e], Tao Xu [a,d,*], Yinshuang Ai [b,d,e], Yingjie Yang [f], Qingdong Zeng [c,d,e], Bing Yu [c,e], Wei Zhang [f], Tongtong Xie [a,e]

[a] State Key Laboratory of Lithospheric Evolution, Institute of Geology and Geophysics, Chinese Academy of Sciences, Beijing 100029, China
[b] Key Laboratory of Earth and Planetary Physics, Institute of Geology and Geophysics, Chinese Academy of Sciences, Beijing 100029, China
[c] Key Laboratory of Mineral Resources, Institute of Geology and Geophysics, Chinese Academy of Sciences, Beijing 100029, China
[d] Innovation Academy for Earth Science, Chinese Academy of Sciences, Beijing 100029, China
[e] University of Chinese Academy of Sciences, Beijing 100049, China
[f] Southern University of Science and Technology, Shenzhen 518055, China

A R T I C L E I N F O

Keywords:
Wulong goldfield
Short-period dense seismic array
Ambient noise tomography
Shallow-crustal velocity structure
Metallogenic potential

A B S T R A C T

Wulong goldfield (WLGF) is situated in the Liaodong Peninsula, northeast of the North China Craton (NCC). During the Mesozoic, the eastern NCC was tectonically reworked, with the stress state to change from compression to extension, accompanied by a large amount of magmatism and extensive gold mineralization. To reveal the relationships among the intermediate to felsic plutons, fault structures, and gold mineralization in the WLGF, we deployed a short-period dense array (WSP array) consisting of 334 portable seismometers. We then processed the ambient noise data to extract a total of 45,531 group velocity dispersion curves with periods of 0.3 to 2.0 s. We adopted a direct inversion method to invert these dispersion curves to construct a 3D ambient noise tomography model of shear-wave velocity structures. The 3D model generated allows us to draw the following conclusions: (1) The model shows prominent NNE- and NW- trending low-velocity anomalies that are interpreted to be caused by the intense hydrothermal alteration related to the gold mineralization along some NNE- and NW-trending faults; (2) The distribution of seismic velocity in the Early Cretaceous Sanguliu pluton in the southern WLGF is not homogeneous on account of its lithological variation, whereby compositional zoning is characterized by monzogranite in the centre and granodiorite in the margin; (3) The concealed NW-trending fault has a larger downward extension (>1.4 km) than that of the NNE-trending faults (~1.0 km), indicating the NW-trending faults played an ore-conducting role and the NNE-trending ones are likely the structures of ore-distributing and/or ore-hosting for the Wulong gold metallogenic system; (4) We suggest three favourable potential areas for future exploration, all of which are located at and around the intersections of the NNE- and NW-trending faults and are close to the known (or concealed) Early Cretaceous granite intrusions; (5) Our results demonstrate that ambient noise tomography based on the short-period dense seismic array is effective in determining metallogenic structures at orefield scale and has significant potential application in mineral exploration.

1. Introduction

The North China Craton (NCC) is the largest and oldest continental block in China, with basement rocks as old as ca. 3.8 Ga (Liu et al., 1992). The NCC is bound to the north by the Paleozoic Central Asian orogenic belt, to the south by the Palaeozoic to early Mesozoic Qinling–Dabie–Sulu orogenic belt, and to the east by the Mesozoic–Cenozoic Circum-Pacific accretionary belt (e.g., Xiao et al., 2003; Miao et al., 2005, Zhai et al., 2002, 2004) (Fig. 1a). Along these tectonic boundaries, gold deposits have been identified, as in comparable settings elsewhere (Groves et al., 1998; Goldfarb et al., 1998). The deposits are typically clustered along the inner margin of the NCC, especially in its eastern part (Fig. 1a).

Numerous studies have examined the gold deposits in the eastern

* Corresponding author at: State Key Laboratory of Lithospheric Evolution, Institute of Geology and Geophysics, Chinese Academy of Sciences, Beijing 100029, China.

E-mail address: xutao@mail.iggcas.ac.cn (T. Xu).

https://doi.org/10.1016/j.oregeorev.2022.104704
Received 22 March 2021; Received in revised form 16 December 2021; Accepted 6 January 2022
Available online 10 January 2022

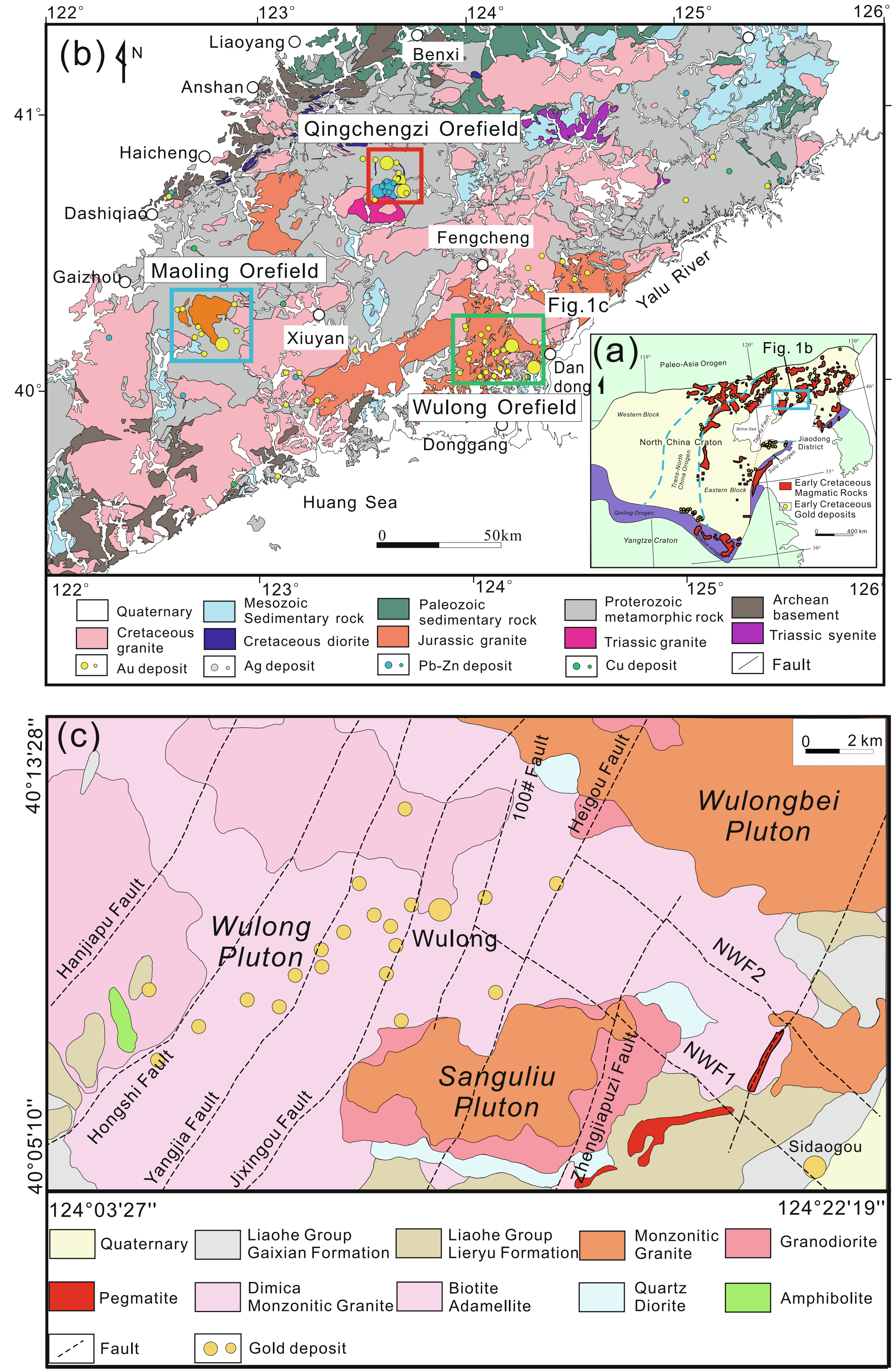

Fig. 1. (a) North China Craton and location of major gold deposits (modified after Zhu et al., 2015). (b) Geological map of the Liaodong Peninsula and distribution of three goldfields. (c) Location and geological structure of the Wulong goldfield (modified after Gu et al., 2020). NWF1, NWF2: NW-trending faults.

NCC, and a consensus regarding the tectonic setting for the formation of gold deposits has been reached. It is considered that they were formed in a tectonic setting of extension or transitional from compression to extension (e.g., Zeng et al., 2019; Deng et al., 2020), which was related to the large-scale lithosphere thinning or decratonisation of the eastern NCC during the late Mesozoic (e.g., Zhai et al., 2002; Zhu et al., 2015; Li et al., 2020). The mineralization time of these gold deposits is ca. 120 ± 5 Ma (Zhu et al., 2015; Li et al., 2020). However, the distribution and metallogenic density of the gold deposits in the eastern NCC, including those on Jiaodong and Liaodong peninsulas, are highly heterogeneous, and the key controls on the heterogeneity remain uncertain.

Jiaodong and Liaodong peninsulas are both located on the northwestern side of the Dabie–Sulu suture zone. They are metallogenically similar, including similar tectonic setting, mineralization characteristics, tectono-magmatic history, and mineralization age (e.g., Li et al., 2015a; Zeng et al., 2019; Deng et al., 2020). Confusingly, the endowment of gold estimated in the two gold districts differs markedly. Jiaodong Peninsula, the largest gold-producing area in China, contains proven gold reserves of > 5000 t (Deng et al., 2020). The proven gold reserves on Liaodong Peninsula are only ca. 500 t (Zeng et al., 2019). In contrast to the intense geophysical exploration of the Jiaodong gold district, exploration of the Liaodong gold district is still ongoing. It is speculated that the deep part of Liaodong Peninsula may have additional gold potential remaining to be identified through further geophysical exploration. This speculation has been reinforced by the discovery of Lode V163, the largest auriferous quartz vein in the Liaodong Peninsula so far. The lode has a strike length of > 1200 m and a vertical extent of 920 m below the surface at an average grade of 6.28 g/t Au (Yu et al., 2018, 2020a). As a result, the deep part below the Liaodong Peninsula has become an important focus of gold exploration.

Ambient noise tomography is regarded as one of the major recent breakthroughs in seismology (Yang et al., 2011). The rapid development of ambient noise tomography during the last two decades has shown that this method is efficient in revealing shallow crustal structures at both regional (e.g., Sabra et al., 2005; Shapiro et al., 2005) and continental scales (e.g., Yang et al., 2007b, 2008a, 2010, 2011). Recently, short-period dense arrays have been developed to image shallow structures rapidly, taking advantage of the low-cost and high-speed characteristics of deployment of ambient noise tomography. Ambient noise tomography based on short-period arrays can identify small-scale faults and geological bodies and thus has been widely used in studies of small regions and/or ore fields (Du et al., 2020; Huang et al., 2010; Li et al., 2016; Lin et al., 2009; Yu et al., 2020c; Fang et al., 2015; Mordret et al., 2019; Roux et al., 2016). For example, Lin et al. (2013) extracted phase velocity dispersion curves from a dense array consisting of 5204 short-period stations in Long Beach, California to inverse a crustal velocity structure of the top 1 km and found that the distribution of the shallow velocity anomalies has a clear correlation with the known faults. Li et al. (2016) combined seismic data obtained from 17 seismometers separated by an average interval of ~ 1.0–2.0 km with borehole data to obtain S-wave velocity measurements from as shallow as 30 m in the Hefei Basin. Wang et al. (2018a) used 203 short-period seismographs deployed in the Xinjiang Basin, Jiangxi Province in China with a spacing of ~ 400 m and obtained a high-resolution velocity structure at 0–1.4 km depths. Du et al. (2020) deployed 100 short-period dense stations with 500–700 m spacing at the Kalatongke Cu-Ni Mine, Xinjiang, to obtain a high-resolution 3D model of structures for a depth range of 0–1.3 km below the mine. Yu et al. (2020c) deployed a linear short-period dense array (including 340 stations) with a spacing of ~ 500 m on Jiaodong Peninsula to obtain a 2D velocity model for depths between 0 and 8 km and investigated the relationship between late Mesozoic extensional structures and gold mineralization in the Jiaodong district. The above studies have demonstrated that ambient noise tomography based on short-period arrays can obtain high-resolution velocity structures of the upper crust and is able to identify ore-controlling structures and plutons in goldfields. Therefore, ambient noise tomography should be of high utility for guiding deep ore prospecting.

To better understand the gold potential in the deep part of Liaodong Peninsula, we performed an ambient noise tomography study in the WLGF by deploying a short-period dense seismic array, which is referred to as WSP array hereafter. The WLGF was selected for our study for the following reasons: (1) The WLGF is the most productive area of gold on Liaodong Peninsula; it contains the largest auriferous quartz vein system and has similar metallogenic characteristics to those of the Linglong gold deposit on Jiaodong Peninsula, both of which host quartz-vein type gold mineralization; (2) Drilling has ascertained that auriferous quartz veins extend vertically to at least 900 m below the surface and a study of structurally superimposed halos suggested a high gold potential in the deeper part of the Wulong gold deposit (Yu et al., 2020b); (3) Geophysical investigations, including gravity, magnetic, and electrical surveys (Gu et al., 2020; Zhang et al., 2019b; Du et al., 2018) provide a good basis for assessing the results of our ambient noise tomography study.

2. Geological setting

2.1. Regional geology

Liaodong and Jiaodong peninsulas including part of the Bohai Sea are part of the "Jiao–Liao Uplift" along the northwestern marging of the Sulu HP–UHP metamorphic belt. This belt is the suture zone between the South China Craton and the NCC. It extends into the Korean Peninsula to the east (Fig. 1).

The basement of Liaodong Peninsula consists of metamorphic rocks of the Archaean Anshan Group and the Paleoproterozoic Liaohe Group. The Anshan Group is mainly distributed in the Liaobei and Liaonan terranes of the Liaodong Peninsula, comprises mainly tonalite-trondhjemite-granodiorite and metamorphosed supracrustal rocks (Liu et al., 1992; Gu et al., 2018; Feng et al., 2020). The Archaean rocks of the Anshan Group host the largest banded iron formation type iron deposit in China.

The Paleoproterozoic Liaohe Group is distributed between the Archaean Liaobei and Liaonan terranes and is considered to represent a sedimentary sequence that formed in the Liaohe Rift. The Liaohe Group is subdivided, from bottom to top, into Langzishan, Lieryu, Gaojiayu, Dashiqiao, and Gaixian formations (Luo et al., 2004; Zeng et al., 2019; Liu et al., 2020a). The Langzishan Formation comprises mainly biotite–chlorite schist and garnet–staurolite–mica schist. The Lieryu Formation has been referred to as a "boron-bearing stratigraphic unit" and consists mostly of magnetite- and tourmaline-bearing gneisses with amphibolite lenses and hosts boron and magnetite deposits. The Gaojiayu Formation comprises predominantly graphite–bearing schists and biotite schists intercalated with marbles, which is the main host rock of lead–zinc deposits on Liaodong Peninsula. The Dashiqiao Formation comprises mainly thick-layered dolomitic marbles, with two-mica schists and carbonacous slate layers. It hosts mineral deposits of magnesite and talc. The Gaixian Formation comprises chiefly phyllite, staurolite–mica schist, sillimanite–two-mica schist, and minor amounts of marbles (Gao et al., 2017; Duan et al., 2014; Li et al., 2015b; Zeng et al., 2019; Liu et al., 2020a). The Liaohe Group underwent greenschist-to amphibolite-facies metamorphism at ca. 1.85 Ga, corresponding to the time of NCC cratonisation (Li et al., 2015b).

The early Precambrian basement of Liaodong Peninsula is unconformably overlain by Neoproterozoic sedimentary rocks of the Yongning Group and Cambrian–Ordovician shallow-marine carbonates and mudstones, which in turn are overlain by Carboniferous–Permian alternating marine- and continental-facies coal-bearing formations. The Yongning Group is characterized by a sequence of wild-flysch formations (Yu et al., 2020a). Mesoproterozoic, Silurian–Devonian, and Triassic strata are absent on Liaodong Peninsula.

Liaodong Peninsula is intruded by granitic rocks of variable ages, including Archaean, Paleoproterozoic, and Mesozoic granites. It should be noted that many granitoids that were previously assigned with Paleoproterozoic ages have subsequently been confirmed to have early Mesozoic emplacement ages (Yang et al., 2008b), meaning that Mesozoic magmatism was more intense and widespread than previously thought. Mesozoic magmatism on Liaodong Peninsula occurred episodically, mainly during the Middle to Late Triassic, Late Jurassic, and Early Cretaceous (e.g., Wu et al., 2005; Yang et al., 2007a, 2012). The Middle to Late Triassic magmatism formed intrusive rocks, without eruptive equivalents, whereas the Late Jurassic and Early Cretaceous magmatism involved both phases. The Late Jurassic–Early Cretaceous volcanic rocks are distributed mainly within Mesozoic faulted basins on the Liaodong Peninsula. It is generally accepted that the collision between the NCC and the South China Craton caused large-scale magmatic activity in the Middle to Late Triassic (Quan et al., 2020), whereas the Late Jurassic–Early Cretaceous magmatism was attributed to the lithospheric thinning or decratonisation of the eastern NCC (Sun et al., 2021; Wu et al., 2005). The westward subduction of the Paleo-Pacific plate beneath the East Asian continent dominated the geodynamics of the lithospheric thinning or decratonisation (e.g., Zhu et al., 2015; Wu et al., 2019; Liu et al., 2020a). Large-scale gold emplacement accompanied the widespread magmatic activity during the Jurassic–Cretaceous, referred by some authors to as the "Mesozoic Metallogenic Explosion" (MME; e.g., Li et al., 2004; Mao et al., 2006; Zhu et al., 2015). The vast majority of gold deposits on both the Liaodong and Jiaodong peninsulas were formed during the MME.

During the Cenozoic, the eastern NCC, including Liaodong Peninsula, experienced the eruption of alkaline basalts with geochemical characteristics of ocean island basalts (Fang et al., 2020). These alkaline basalts are sparsely distributed along major NE-trending faults.

2.2. Geology of the WLGF

According to the time–space distribution and metallogenic characteristics of the gold deposits, Liaodong Peninsula is divided into three areas of gold concentration: the Qingchengzi, Maoling, and Wulong goldfields (Zeng et al., 2019). The Qingchengzi goldfield is located in northern Liaodong Peninsula and hosts several gold deposits, such as the Baiyun, Xiaotongjiapu, and Linjiasandaogou (Liu et al., 2020a). The Maoling goldfield includes several large gold deposits (such as Maoling) and other smaller deposits and occurrences (Yu et al., 2020a; Zhang et al., 2017). The WLGF hosts two large-scale gold deposits, Wulong and Sidaogou, as well as some small-scale gold deposits and occurrences (Feng et al., 2019; Yu et al., 2020a). Among these, the Wulong gold deposit is the most important, with>80 t of Au at an average grade of 5.35 g/t (Yu et al., 2020a; Fig. 1a). The gold deposits in the WLGF are mainly of quartz-vein type, whereas the disseminated and stockwork style of gold mineralization hosted in altered tectonic zones has also been found nearby.

Country rocks of the deposits in the WLGF belong to the Paleoproterozoic Liaohe Group and the Neoproterozoic Yongning Group (Zeng et al., 2019). For the Liaohe Group, only the Lieryu and Gaixian Formations are present and are distributed in the southeastern part of the WLGF, and the Gaixian Formation comprises predominantly mica schist. The Yongning Group, composed of quartz sandstone, is distributed near the Sidaogou gold deposit in the southeast of the WLGF (Duan et al., 2014; Yu et al., 2020a).

The WLGF is intruded by Mesozoic granitic rocks, with the Wulong, Sanguliu, and Wulongbei plutons being the main representatives. The Wulong pluton, emplaced in the Late Jurassic with a zircon U–Pb age of ~ 160 Ma, is widely distributed in the WLGF and is mainly composed of two-mica granite and biotite granite (Wang et al., 2019; Wu et al., 2005; Yu et al., 2020a). The Sanguliu pluton in the southeastern portion of the goldfield is composed of monzogranite and granodiorite and shows lithological zoning, with the monzogranite in the centre and the granodiorite (as well as a minor amount of quartz diorite) at the margin. Zircon dating has revealed that the central monzogranite and marginal granodiorite were formed simultaneously, with emplacement ages of 131–120 Ma (Early Cretaceous) (Wang et al., 2020). The Wulongbei pluton in the northern part of the goldfield is a monzonitic granite and shows a porphyritic structure. This pluton was emplaced during the Early Cretaceous as indicated by its zircon U–Pb age of 127 $\pm$ 5 Ma (Wu et al., 2005).

There are two groups of faults that were mapped in the WLGF, which extend NNE and NW, respectively (Yu et al., 2018; Zhang et al., 2020). Of these, the NNE-trending group of faults is predominant and is widely distributed in the WLGF. The NNE-trending faults, interpreted as subsidiary faults of the Yalujiang Fault to the southeast of the goldfield, strike about 25–30° and dip to the NW, with steep dip angles of 50°–80° (Zhang et al., 2019b). The NW-trending faults are only locally exposed in the northeastern WLGF and show a general strike of about 320° and dip to the SW at 50–70° (Gu et al., 2020; Zhang et al., 2019b). These two groups of faults, which are considered to be conjugate, constitute the main structural framework of the WLGF and control the spatial distribution of gold deposits (Gu et al., 2020).

2.3. Geology of the Wulong gold deposit

The Wulong gold deposit is situated in the northwestern part of the Sanguliu pluton (Fig. 1). Besides the granitic plutons, there are many dikes of different composition and orientation. These dykes are mainly Early Cretaceous in age (Yu et al., 2020a) including fine-grained diorite, granitic porphyry, dolerite, and lamprophyre. The fine-grained diorite dykes strike mainly NNE, NW, or N. The granitic porphyry dykes (>2 m wide and thousands of meters long) strike N or NNE and are distributed mainly in the east of Wulong. The lamprophyre and dolerite dykes (~1 m wide and > 10 m long) strike N or E. In addition, some diorite porphyry and granitic pegmatite dykes are also found in the deposit. The granitic porphyry and fine-grained diorite dykes generally crosscut the auriferous quartz veins (Yu et al., 2020a) suggesting their emplacement postdating the gold mineralization.

The Wulong orebodies are chiefly distributed in between the Jixingou and 100# Faults, two major regional NNE-trending faults (Fig. 2). Nevertheless the orebodies are directly hosted by small-scale faults that are different in orientation from the regional faults. It is suggested that the sinistral movement on the Jixingou and/or 100# Faults has led to many small-scale subsidiary faults (generally less than 1 km long) that strike N5-15°NE (dipping to the W at angles of 75–85°) or NW (dipping to the SW at angles of 50–70°). The Wulong auriferous quartz veins hosted by these subsidiary NNE- and NW-trending faults have been identified as occurring in belts (groups) with different dimensions. The largest orebody of the Wulong gold deposit is the NW-trending Lode V163 (dipping to the SW), which has a length of>1200 m and a width of>10 m, with an average gold grade of 6.28 g/t Au (Wang et al., 2018b; Yu et al. 2018, 2020a; Zhang et al. 2019a).

3. Shallow-crustal velocity structure of the WLGF

3.1. Data and methods

(1) Ambient noise data-processing

The data used in this work are ambient noise data obtained from the short-period dense array in the WLGF (WSP array, Fig. 2), including 334 three-component seismometers, deployed from May to June in 2019. The array covers almost all of the faults and gold deposits. The WSP array is ~ 27 km long and ~ 7 km wide, with an average distance of 0.5–1 km between stations. The original sampling rate of ambient noise seismic data is 250 Hz.

We processed the ambient noise data according to the processing procedure of Bensen et al. (2007). Data were cut into 1 h segments and resampled at 10 Hz. Subsequent steps involved de-meaning, de-trending, bandpass-filtering the seismogram at 0.3–10.0 s periods, time-domain normalizing and spectral whitening. We still removed the

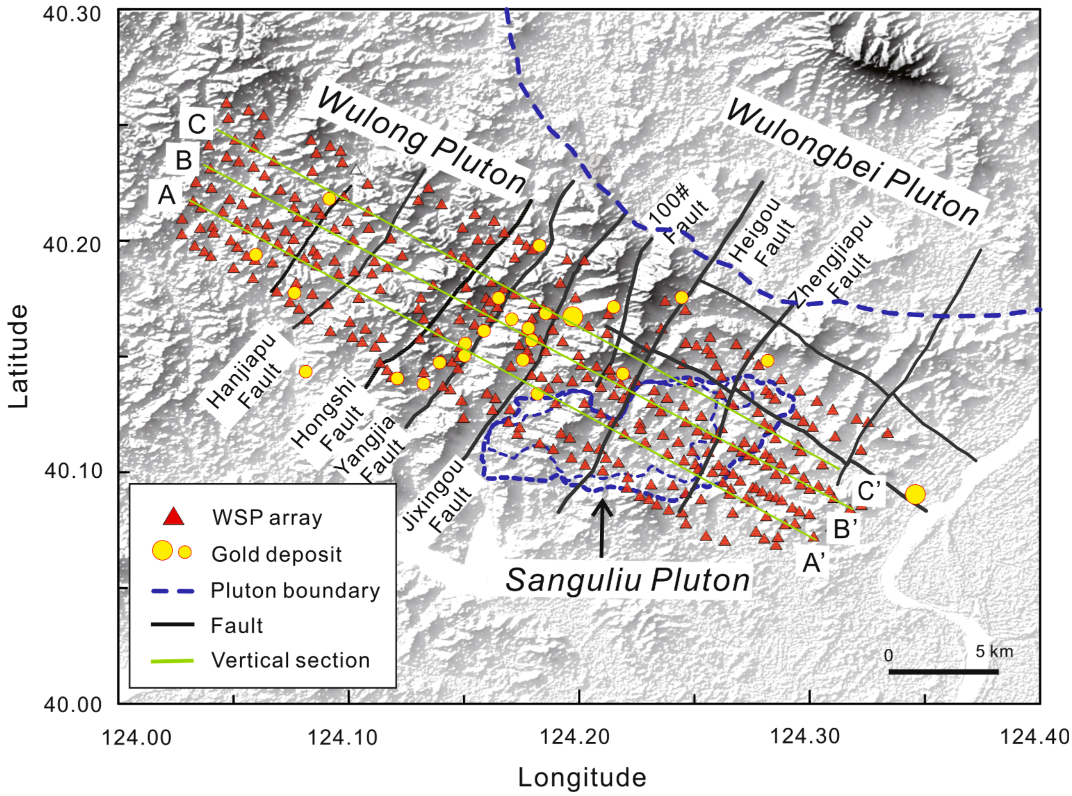

Fig. 2. Topography of the Wulong goldfield, Liaodong Peninsula, China along with the main geological structures. AA', BB', CC' are the locations of three vertical sections.

instrument response, even though our instruments were the same.

We cross-correlated the processed 1 h data between available stations and stacked corresponding 1 h cross-corrections for each station pair to obtain stacked noise cross-correlation functions (NCFs). Finally, we obtained 55,611 NCFs. Fig. 3 presents the NCFs between station WL100 and other stations and reveals that Rayleigh surface wave signals with an apparent velocity of about 3.0 km/s can be observed clearly at a period band of 0.3–2.0 s (Fig. 3a). In contrast, the NCFs at period bands of 2–5 s (Fig. 3b) and 5–10 s (Fig. 3c) appear to have strong noise at zero lag time. Therefore, we measured dispersion curves from the NCFs only at the period range of 0.3–2.0 s.

(2) Rayleigh wave group velocity dispersion measurement

Rayleigh wave group velocity dispersion curves were extracted based on a rapid image analysis extraction method (Yao et al., 2006). This method is based on a visual interface and can automatically extract a large number of dispersion curves and check the accuracy of dispersions. We measured the group dispersion curves only from those NCFs that had signal-to-noise ratio values of >5 and distances between two stations longer than two wavelengths. In the automatic extraction, the average velocity obtained from 1000 manually picked curves was taken as the reference velocity. We discarded group velocity dispersion curves with perturbations>0.2 km from the reference velocity. Finally, 49,211

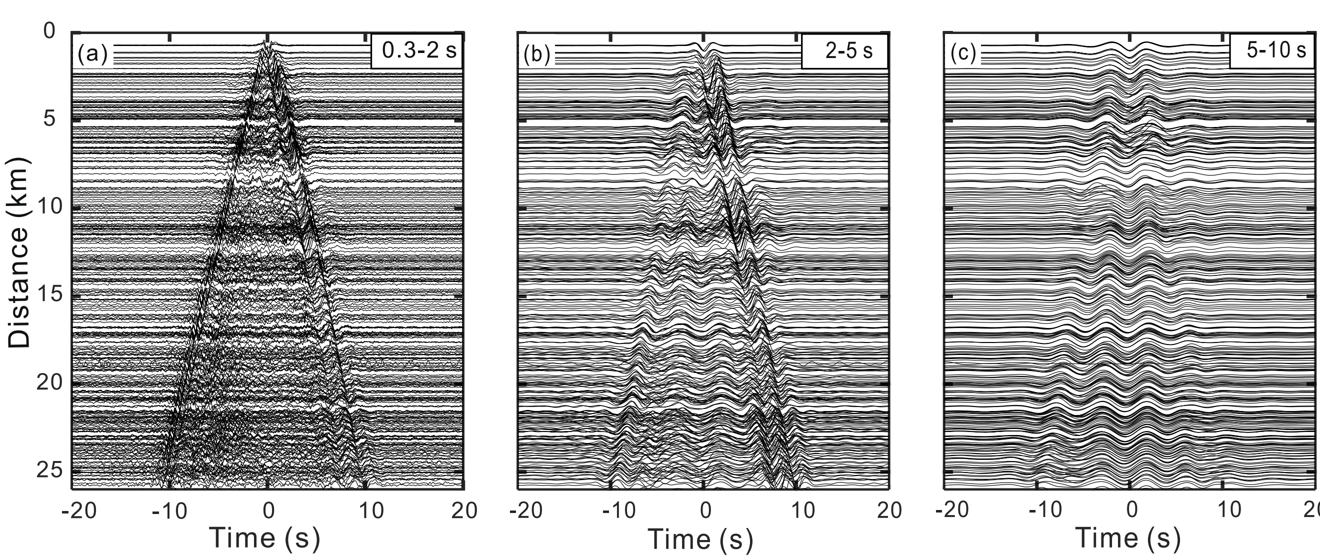

Fig. 3. Cross-correlation functions of station WL100 with other 333 stations filtered at period band of (a) 0.3–2 s; (b) 2–5 s; and (c) 5–10 s.

group velocity dispersion curves were automatically extracted.

We found that some of the automatically picked dispersion curves were not smooth and had large oscillations according to period. However, dispersion curves must smoothly vary as a function of period. Therefore, further selection steps were implemented to discard the problematic dispersion curves. Here, we adopted a similar propagation path method to identify and discard these problematic dispersion curves manually. The main principle behind this method is that if the propagation paths of surface waves are similar, their dispersion curves must also be similar. To find similar paths, we first chose two stations as central stations and then drew two circles centred on each of the two stations with a certain radius. Then, we chose station pairs with one station located within one circle and the other station located in the other circle and treated all paths from these station pairs as similar paths. For cases where the distance between two central stations was less than 6 km, we took one-sixth of the distance between the two central stations as the radius to draw the two circles. For cases where the distance between two central stations was>6 km, we took 1.2 km as the radius. Then, all dispersion curves from the same similar paths were plotted as reference dispersion curves (blue line in Fig. 4a) to judge whether the dispersion curve from the central station pair (red line) should be retained or discarded (Fig. 4a). If the dispersion curve from the central stations was located outside the corridor of the reference dispersion curves, then that dispersion curve was discarded.

Following the above procedures, we took each of the available station pairs as the central station pair to judge whether it was reliable. Finally, 45,531 group velocity dispersion curves were retained (Fig. 4b). Fig. 4c shows the number of dispersion curves for each period. Among them, there are>30,000 dispersion curves for each period less than 1.2 s, indicating that the data are highly suitable for tomography (Fig. S1 in the Supporting Information).

(3) Direct inversion for shear-wave velocity

We adopted the direct inversion method developed by Fang et al. (2015) to invert our dispersion data for 3D shear-wave velocity. This method employs ray tracing based on frequency and sparse constrained tomographic inversion based on wavelet, without an intermediate inversion step. We used a fast matching method (Rawlinson and Sambridge, 2004) to forward the accurate 3D shear-wave velocity model. This forward method can be used to calculate the ray paths and travel time between earthquakes and receivers.

LSQR (least squares QR-factorization) algorithm (Paige and Saunders, 1982) was used to solve the inversion. The objective function is presented as follows:

$$\Phi(\boldsymbol{m}) = ||\boldsymbol{d} - \boldsymbol{Gm}||_2^2 + \lambda||\boldsymbol{Lm}||_2^2 \tag{1}$$

where $\boldsymbol{d}$ is the travel time, $\boldsymbol{L}$ is the smoothing operator, $\boldsymbol{G}$ is the sensitive kernel function, m is the model parameter, and λ is the weight factor between the data residual and the model regularization. In inversion, the selection of λ is very important. If it is too small, the weight of the data residual will be excessive, overfitting data during inversion, resulting in unsmooth results, and mapping data residuals into the results; in contrast, if λ is too large, the results will be too smooth, lacking a fine velocity structure. Therefore, to determine a reasonable λ value, we tested different values of λ (from 3 to 100) and plotted an L-curve (Fig. 5). The weight at the inflection point of 10 was picked as the optimal λ value for our inversion.

(4) Resolution tests

To test the robustness of our inversion results, resolution tests were performed. Fig. 6 shows the distribution of ray paths and the sensitive kernels of Rayleigh wave group velocity at different periods, from which it can be shown that the ray path coverage at periods of 0.3–1.5 s is dense, with corresponding sensitive depths of 0.25–1.50 km. The area with the densest coverage of paths is around the WLGF, where numerous faults are developed.

A checkboard resolution test is an effective way to examine the size

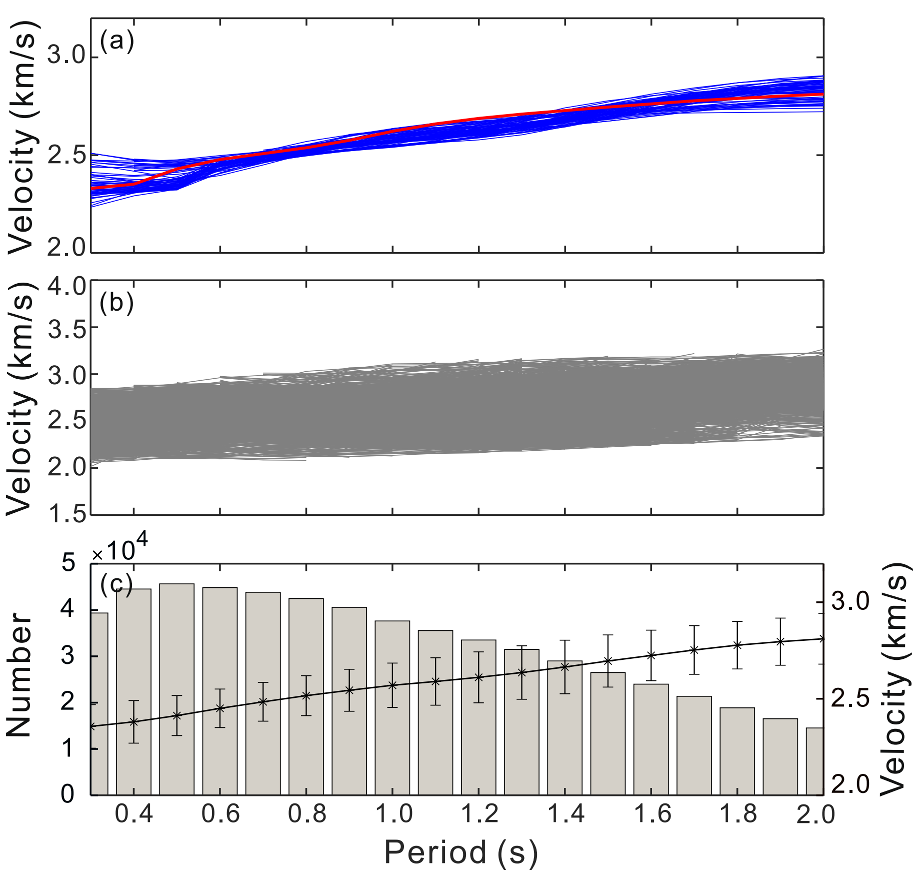

Fig. 4. Results of group velocity dispersion curves. (a) Examples of dispersion curves under the same similar propagation path (red line: dispersion curve of central station pair; blue line: reference dispersion curves). (b) Group velocity dispersion curves (45,531 in total) obtained by the similar propagation path method. (c) The number of dispersion curves at each period. The black line is the average dispersion curve with standard deviations plotted as error bars to represent the variation in our measured group velocity across the study area.

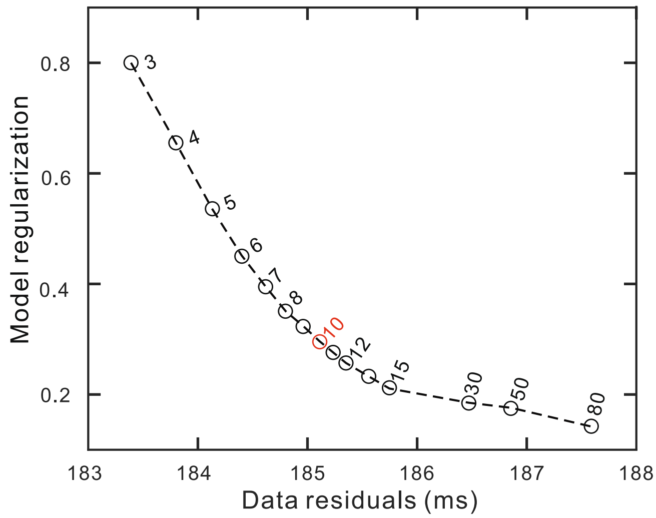

Fig. 5. L-curve obtained from using different λ values. The optimal value is 10 as indicated by the red circle.

of the resolvable abnormal body in tomography. We performed horizontal and vertical checkboard resolution tests, and the results revealed that our dataset has a lateral resolution of ~ 2 km and a vertical resolution of ~ 0.4 km at shallow depths (less than1.2 km) (Figs. S1 and S2). The variation in travel-time residuals before and after the inversion also indicates the reliability of the results (Fig. S3). More detailed results are provided in the Supplementary Information.

3.2. Results

In accordance with the empirical relationship proposed by Shearer (2019), we established an initial 1D velocity model for our inversion (Fig. 7). The depth of the initial model was extended to 3.0 km to avoid boundary effects and stabilize the inversion. Model parameterization in the direct inversion method followed the model presented by Boschi et al. (2020), and the velocity and density of P-waves were obtained from the empirical relationship determined by Brocher (2005). For the inversion, the grid node sizes in the latitude and longitude directions were both 0.015° (~1.6 km), and the node interval in the depth dimension was ~ 200 m. To check the stability of the algorithm, we tested a number of initial models; these tests showed that the initial model had only weak effects on the results and that the algorithm was relatively stable (refer to the Supplementary Information).

After the inversion, we obtained velocity structures within 1.5 km depth below the surface in the WLGF. Fig. 8 shows horizontal slices of S-wave velocities at depths of 0.26, 0.44, 0.65, 0.84, 1.05, and 1.26 km, respectively. Fig. 9 presents vertical transects of the velocity structures (locations of the transects are shown in Fig. 2).

Figs. 8 to 10 reveal that the velocity structure below the WLGF has the following features:

1) A NNE-trending low-velocity zone (No. L1) (Fig. 8) is pronounced near the Jixingou fault and vertically extends at least to 1 km depth;

2) A distinct NW-trending low-velocity zone (No. L2) traverses the whole goldfield and extends down to a depth of > 1.26 km underneath the surface;

3) Two low-velocity anomalies (L3 and L4) exist around the western and eastern margin of the Sanguliu pluton, respectively, with both extending to a depth of > 1.26 km below the surface; interestingly, the locations of anomalies L3 and L4 gradually shift to the northeast and north, respectively, with increase of depth.

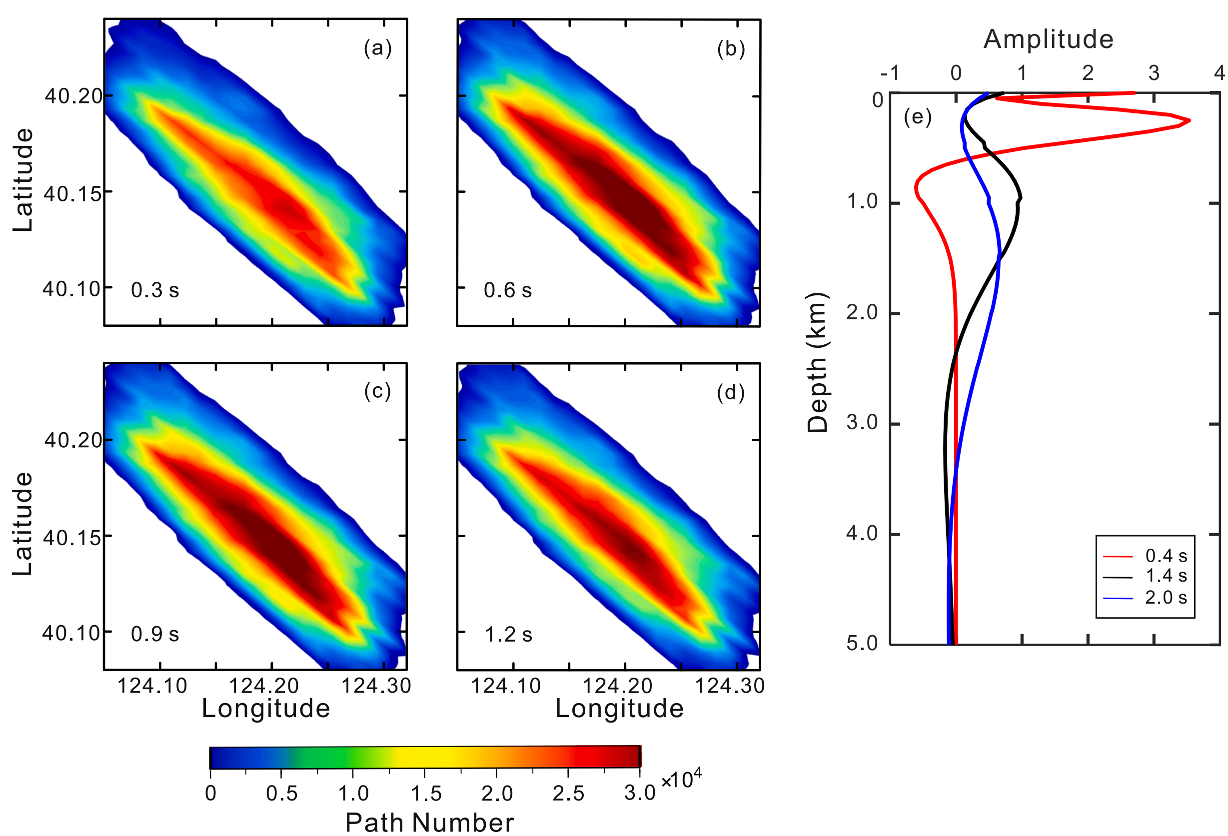

Fig. 6. (a-d) Distribution maps of ray paths at different periods. (e) Rayleigh wave group velocity depth sensitivity kernels at different periods. Red line is 0.4 s; black line is 1.4 s; blue line is 2.0 s.

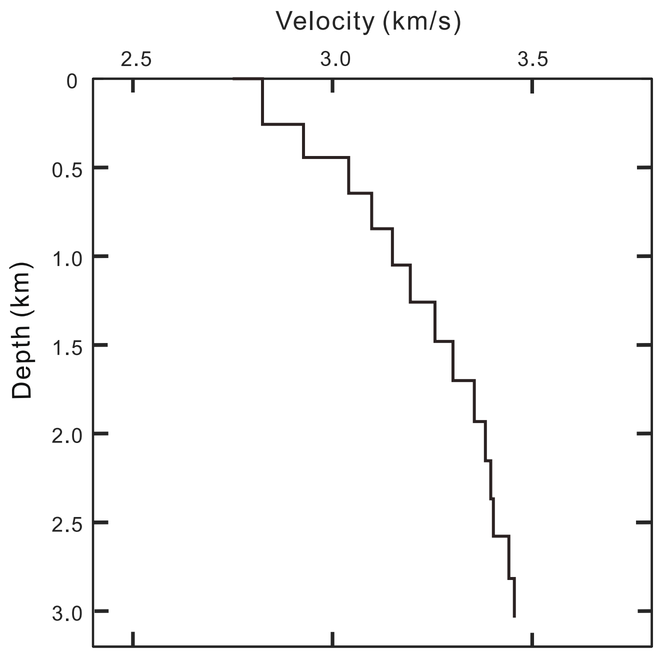

Fig. 7. 1-D initial velocity model.

4. Discussion

4.1. Interpretation of the 3D model

As mentioned above, the most attractive feature of the shallow crust structure of the WLGF is the existence of several evident low-velocity anomalies (L1-L4; Fig. 8). These low-velocity anomalies may represent different geological features. The L1 anomaly in the central part of the WLGF is generally NNE-trending and is broadly coincident in plan with the area between the NNE-trending Yangjia and 100# faults. Although regional fault zones generally show a low-velocity feature due to faulting leading to lithofraction and fragmentation within them, we interpret the L1 anomaly to be caused mainly by the extensive and intensive hydrothermal alteration (water-bearing minerals) that was likely related to the formation of the Wulong gold deposit, as well as other smaller deposits and occurrences. The reasons for this are two-fold. One reason is that not all of the NNE-trending faults in the goldfield show a low-velocity anomaly feature, indicating that the velocity anomaly can not be attributed only to the faults. At the same time, the L1 and L3 anomalies seem to connect to each other to constitute one single low-velocity anomaly extending along the whole of area between the Yangjia and 100# faults above 400 m depth below the surface but they are obviously separated below that depth (Fig. 8), similarly suggesting that fault is not the dominant factor generating the L1 anomaly. The other reason is that the largest gold deposit (Wulong) and several other smaller deposits and occurrences in the WLGF occur within the L1 anomaly, with Wulong occupying the center (Fig. 8), implying that strong wallrock alteration might take place within and below the area of the L1 anomaly.

For the L2 anomaly, which occurs as a straight NW-trending zone nearly transverse the whole WLGF, we similarly interpret it to result from intense hydrothermal fluid alteration along one or two NW-trending faults. However, there are no such NW-trending faults were observed in the central-western part of the goldfield and there are no lithological interfaces that are in agreement with the L2 anomaly in orientation. Therefore, considering the straight stretching feature of the L2 anomaly, we infer that anomaly L2 represents a buried NW-trending fault, along which the hydrothermal alteration related to the gold mineralization occurred, and thus leading to an evident low-velocity zone. The coincidence of a known NW-trending fault (NWF1) with the

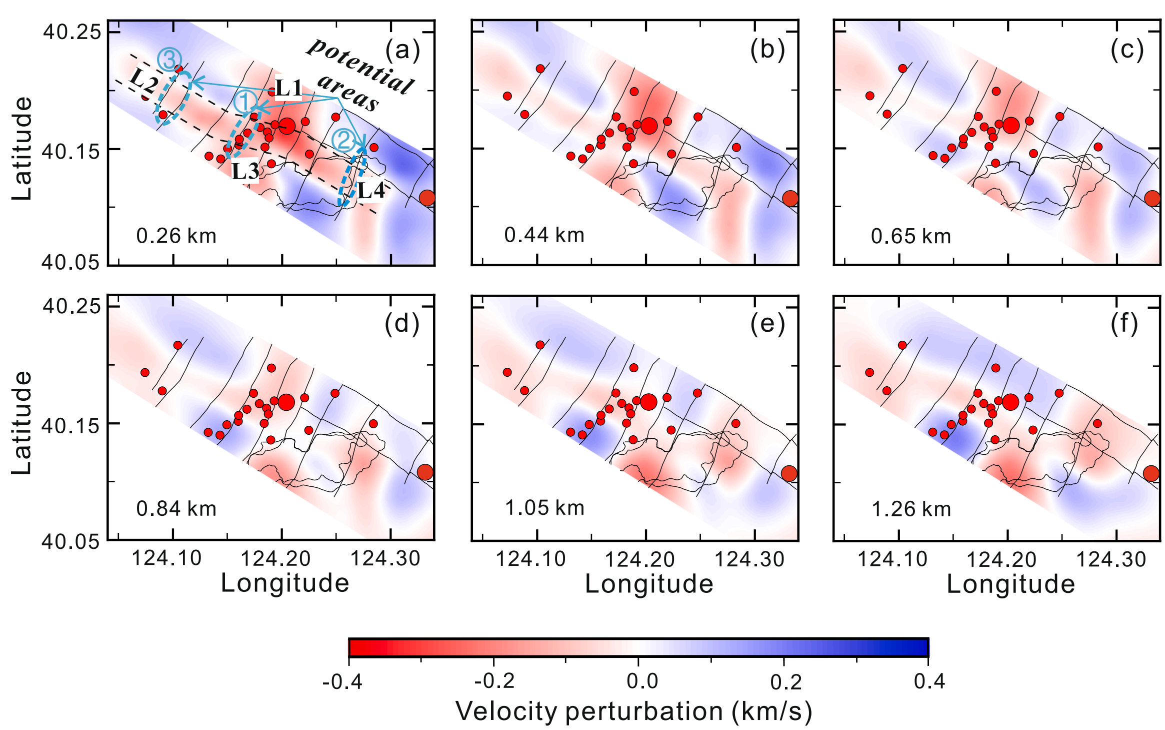

Fig. 8. Relative shear-wave velocity slices at different depths obtained by the direct inversion method: a) 0.26 km, b) 0.44 km, c) 0.65 km, d) 0.84 km, e) 1.05 km, and f) 1.26 km. The red solid dots denote the gold deposits and occurrences, and the largest ones present the Wulong gold deposit and the Sidaogou gold deposit; the black solid lines correspond to the known faults; the closed black line in the southeast presents the Sanguliu pluton with monzonitic granite inside and granodiorite outside; the black dashed lines in Fig. 8a indicate the boundary of the NW-trending low-velocity zones; These blue circles in Fig. 8a indicate the potential metallogenic areas; L1-L4: low-velocity zones.

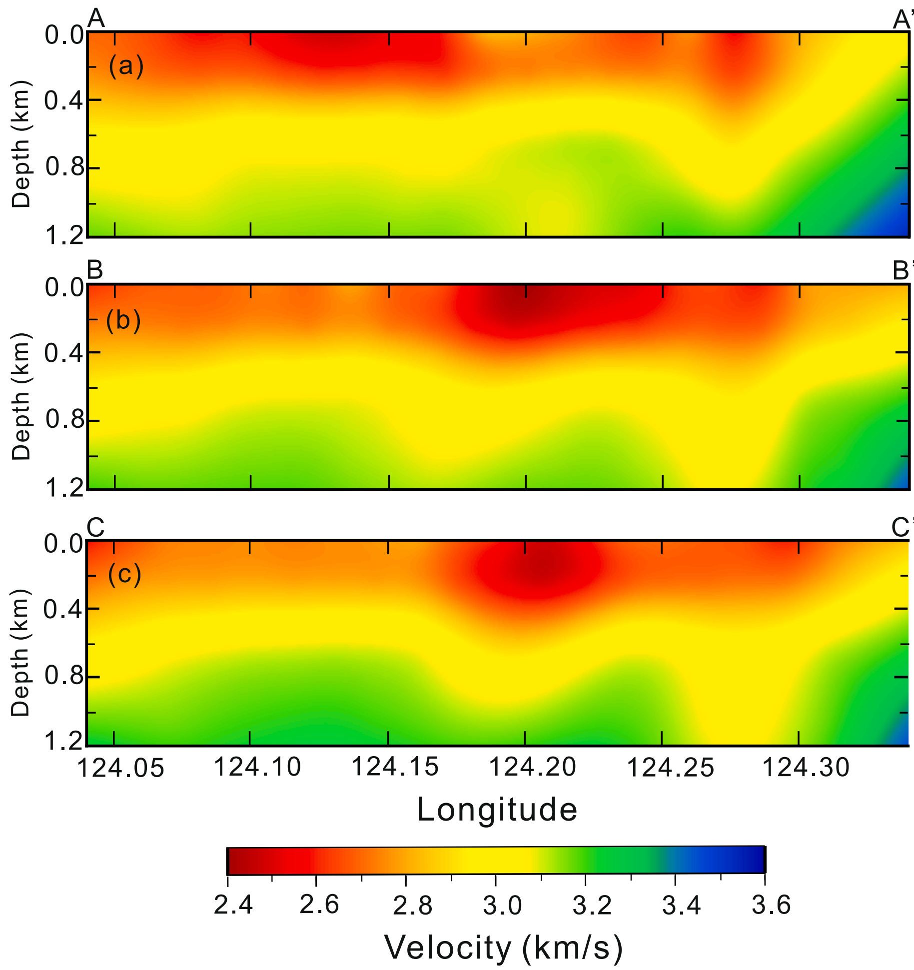

Fig. 9. Vertical transects of velocity structures with the surface sections shown in Fig. 2.

northern boundary of the L2 anomaly in the northeastern WLGF (Fig. 8) also supports our suggestion. In addition, previous geophysical studies also identified a NW-trending magnetotelluric and magnetic anomaly that is generally consistent with the L2 low-velocity anomaly and was considered as a buried fault zone (Zhang et al., 2019b). Consequently, we urge that the observed NW-trending L2 low-velocity zone represents one or two NW-trending fault zones that are buried under Cenozoic sediments, in which intense hydrothermal alteration occurred likely during the Early Cretaceous. It is noted that the vertical extent of the L2 anomaly is obviously greater than that of the L1 one. This likely suggests that the buried NW-trending fault and/or its alteration extent are vertically greater than the NNE-trending ones.

The L3 and L4 anomalies are located on the western and eastern margins of the Sanguliu pluton, respectively (Fig. 8). This distribution pattern is generally consistent with that of the lithological variation of the pluton (Figs. 8 and 10). For example, on the eastern and western margins of the Sanguliu pluton, granodiorite and quartz diorite are the main components and exhibit lower shear-wave velocity compared with monzogranite in the central part of the pluton. This can be explained by the higher contents of water-bearing minerals (e.g., hornblende) in the granodiorite and quartz diorite relative to the monzogranite. Additionally, the results of inversion of gravity and magnetic data are consistent with the distribution of velocity in the Sanguliu pluton, that is, the negative gravity and magnetic anomalies in the center are representative of Early Cretaceous granite, while the positive gravity and magnetic anomalies at the two edges of the pluton indicate Early Cretaceous granodiorite (Zhang et al., 2019b). Therefore, we interpret the velocity structure in and around the Sanguliu pluton is likely controlled by lithological differences, with the L3 and L4 anomalies caused by amphibole-bearing dioritic rocks. Some contribution of the hydrothermal alteration associated with the gold mineralization to the L3 and L4 anomalies is also possible because the Sanguliu pluton is genetically related to gold mineralization (Yu et al., 2020a), leading to hydrothermal alteration along its margins, especially when faults exist on the margins (e.g., the Zhengjiapuzi fault is parallel to and cuts through its eastern margin).

In a word, the crustal shear-wave velocity structures beneath the WLGF are characterized by several low-velocity anomalies showing different orientations and extents. The L1 and L2 anomalies likely reflect the exposed or concealed regional faults that might have been superimposed by intense hydrothermal alteration accompanying gold mineralization. The L3 and L4 anomalies are ascribed mainly to the difference in lithology of the composite Sanguliu pluton though the contribution of the hydrothermal alteration can not be precluded.

4.2. Implications for exploration potential

As aforementioned, the gold mineralization in the WLGF is dominated by the quartz-vein type and the ore-forming fluids are mainly magmatic in origin, with some addition of paleo meteoric water in the late-stage mineralization (Zeng et al., 2019; Yu et al., 2020a). The gold deposits were formed in the Early Cretaceous (ca. 125–120 Ma) and were genetically related to the coeval granitic magmatism generating plutons that are presently either exposed on the surface (e.g., the Sanguliu pluton) or buried underground (Zeng et al., 2019; Yu et al., 2020a, b). On the regional/goldfield scale, the gold deposits as well as

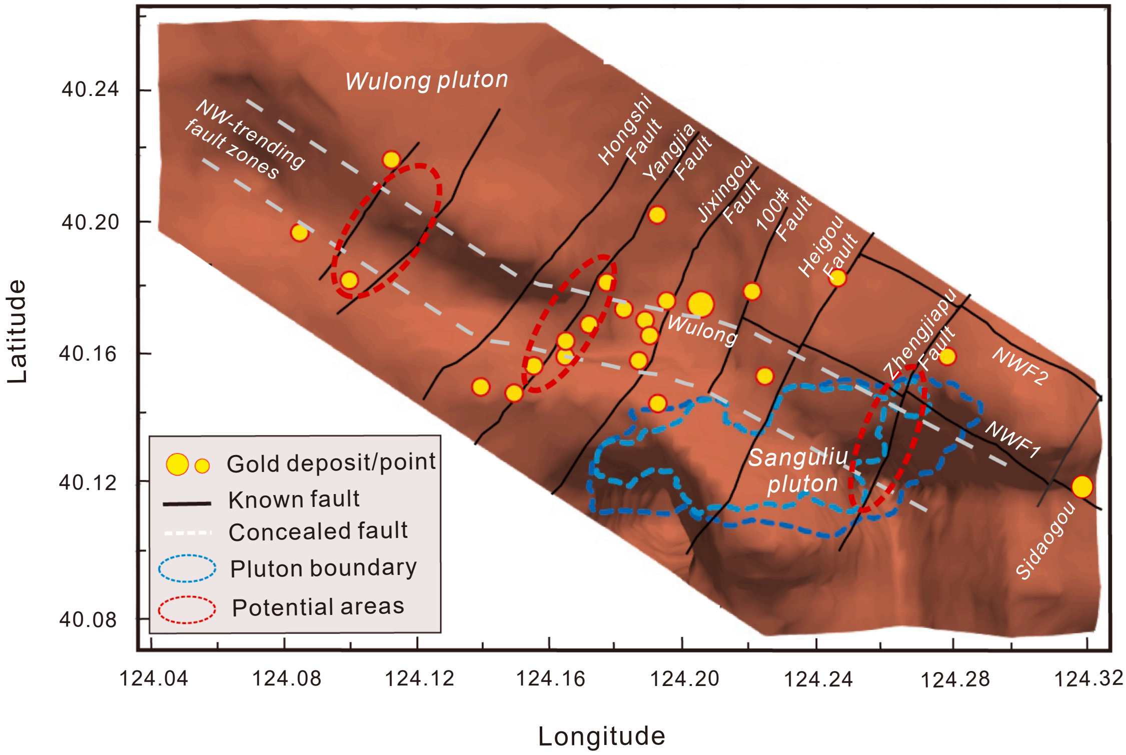

Fig. 10. The 3D shallow crustal structure of the Wulong goldfield. The isosurface corresponds to a velocity of 3 km/s, and the depth is within 1.2 km. The white dotted lines indicate the NW-trending concealed faults we found. These red circles indicate the three potential metallogenic areas we speculate for future exploration, all of which are located at and around the intersections of the NNE- and NW-trending faults and are close to the known (or concealed) Early Cretaceous granite intrusions. NWF1, NWF2: NW-trending Fault.

occurrences seem to be distributed within or around several regional faults that cut through late Mesozoic granitic intrusions (e.g., Wulong gold deposit) and Precambrian metamorphic rocks of the Liaohe Group (e.g., Sidaogou gold deposit) (Fig. 1c and 2; Yu et al., 2020a). Nevertheless, on a scale of individual gold deposits, the orebodies/gold-bearing quartz veins are actually hosted directly by the NNE-, NE-, N- and NW-trending secondary-order faults developing beside the regional NNE-trending faults, which is particularly evident at the Wulong deposit (Zeng et al., 2019). Importantly, the 163# gold-bearing quartz vein at the Wulong gold deposit has been confirmed by drilling to extend down to at least 1.4 km deep below the surface and the gold mineralization is still economically significant at that depth. This suggests that the deep part (at least above 1.4 km depth) of the goldfield has a high potential for gold metallogeny. In addition, gold mineralization with 2.12 g/t Au has been discovered inside the NNE-trending Jixingou Fault zone (Yu et al., 2020b). These indicate that not only the secondary splay faults of the NNE-trending regional faults but also the NNE-trending regional faults themselves are likely the main ore-hosting structures of the gold metallogenic system, showing their high gold potential.

Generally, our ambient noise tomography results are in agreement with the essential geological features of the goldfield and corroborate the conclusion of the high gold potential below the WLGF. On the one hand, our ambient noise tomography results reveal the general structural framework that might have controlled the gold mineralization. As discussed in the last subsection, the hydrothermal alteration along the buried NW-trending fault(s) has a larger vertical extent than that along any of the NNE-trending ones, implying that the former probably played a role of the ore-conducting structure of the Wulong gold metallogenic system and the latter the ore-distributing, or ore-hosting, structure. Considering the fact that majority of the gold-bearing quartz veins are directly hosted in the second order fractures beside the regional NNE-trending faults, the final ore-hosting structure, it is evident that the structural configuration is favorable to the gold metallogeny (Liu et al., 2018). On the other hand, our ambient noise tomography results indicate that just a few of faults show low-velocity anomalies, possibly suggesting selective hydrothermal alteration and/or gold mineralization, meaning that the alteration and gold mineralization has been concentrated in the areas below these faults. Obviously, the deep part of these faults should have high metallogenic potential.

In terms of spatial relationship of the gold deposits and the low-velocity anomalies, it is evident that most known gold deposits and occurrences in the WLGF are spatially distributed within the scope of the L1 and L2 low-velocity anomalies (Fig. 8a). Meanwhile, the intersection of the two anomalies is likely the preferred area for gold mineralization, with the majority of gold deposits occurring there, which implies that the intersections of the NNE- and NW-trending regional faults are likely to play a key role in controlling the distribution of the gold deposits. This is specifically true for the Wulong and Sidaogou gold deposits, the two biggest deposits in the goldfield, both of which are located near the fault intersections (Fig. 1c and 8). We urge that there is a large potential exploration space in the deep part of the WLGF. Apart from the deep part of the Wulong gold deposit, where the existence of economic gold mineralization has been attested by drilling, we propose other three potential metallogenic areas for future exploration (Fig. 8a).

The first potential area is located about 3 km southwest of the Wulong gold deposit. The reasons for selecting this area are as below: 1) it belongs to the intersection region of the L1 and L2 low-velocity anomaly zones; 2) it is located in detail at and around the intersection of the NNE-trending Yangjia Fault with the L2 low-velocity anomaly zone; 3) several small-scale gold deposits and occurrences have been delineated on the surface and/or shallow level of the area; 4) this potential area is located to the northwest of, and not far from, the Early Cretaceous Sanguliu pluton that has a genetic relation to the gold mineralization.

The second potential area is located at about 7 km southeast of the Wulong gold deposit. The favourable conditions for choosing this area mainly include that it is situated around the intersection of the NNE-trending Zhengjiapuzi Fault and the known NW-trending NWF1 that occurs along the northern boundary of the L2 anomaly zone (Fig. 8), and that it is directly located at the contact of the Sanguliu pluton. Additionally, this area is at or around the midpoint of the NWF1 segment between the Wulong and Sidaogou deposits, implying a high possibility of the gold mineralization provided that the equidistant distribution of gold deposits exists in the WLGF, like that recognized in the Linglong goldfield in the Jiaodong Peninsula (Wen et al., 2015).

The third potential area is situated around the intersections of the L2 anomaly zone with the two NNE-trending faults in the northwest of the WLGF, (Fig. 8). Selection of this area as a potential one is mainly due to its location within the L2 anomaly and several gold occurrences have been discovered in the area. In addition, although this area is far from the Early Cretaceous Sanguliu pluton and there are no low-velocity anomaly zones along the segments of the two NNE-trending faults outside the L2 anomaly, which seems to be unfavorable for the gold mineralization, the intensity of low-velocity of the area gradually increased with increasing depth compared with the adjacent segments of the L2 anomaly (Fig. 8b). This may indicate another fluid activity and/or gold mineralization center existing below the area. Meanwhile, it appears that this center gradually migrates to the south with increasing depth. The idea of the existance of the center is consistent with the suggestion that deeply concealed Early Cretaceous plutons might have provided partial ore-forming fluids for the Wulong gold metallogenic system (Zeng et al., 2019; Liu et al., 2020b).

In summary, the L1 and L2 low-velocity anomalies reflect the hydrothermal alteration and/or gold mineralization along the NNE- and NW-trending faults and their intersection is the favorable for gold mineralization. The three areas suggested, based on our new ambient noise tomography results as well as published data, for the future exploration are all associated with these anomalies and are located at the intersections of the NNE- and NW-trending faults.

5. Conclusions

Our investigation of the Wulong goldfield, Liaodong Peninsula, using ambient noise tomography with a short-period dense array, allows us to reach the following conclusions.

(1) The shallow crustal shear-wave velocity structures beneath the WLGF are characterized by the existence of mainly 4 low-velocity anomalies (L1-L4) of different dimensions and orientations: the L1 anomaly as a wide band extending along the northern part of several NNE-trending faults in the central-northern WLGF; the L2 anomaly as a narrow zone transverse nearly the whole WLGF in a NW direction; and the L3 and L4 anomalies as relatively rounded bodies occurring on the western and eastern margins of the Sanguliu pluton in the central-southern WLGF.

(2) The L1 and L2 anomalies are interpreted to be caused by the intense hydrothermal alteration related to the gold mineralization along some NNE- and NW-trending faults, respectively, whereas the L3 and L4 anomalies difference in lithology of the two margins from the central part the Sanguliu pluton, an Early Cretaceous composite intrusion that is considered to be genetically related to the gold mineralization.

(3) The L2 anomaly zone, which is interpreted to reflect the existance of one, or two, NW-trending faults concealed by young sediments, has a larger downward extension (>1.4 km) than that of the L1 anomaly (~1.0 km), indicating the NW-trending faults played an ore-conducting role and the NNE-trending ones are likely the structures of ore-distributing and/or ore-hosting for the Wulong gold metallogenic system.

(4) According to the spatial distribution of the known gold deposits/occurrences and the velocity anomalies, together with the gold metallogenic model, we suggest three favourable potential areas for future exploration, all of which are located at and around the intersections of the NNE- and NW-trending faults and are close to the known (or concealed) Early Cretaceous granite intrusions.

(5) Our results demonstrate that ambient noise tomography based on the short-period dense array is effective in determining metallogenic structures at orefield scale and has significant potential application to mineral exploration.

Declaration of Competing Interest

The authors declare that they have no known competing financial interests or personal relationships that could have appeared to influence the work reported in this paper.

Acknowledgments

We extend our thanks for the great efforts of the Liaohe Geophysical Exploration Company, Bureau of Geophysical Prospecting INC., and China National Petroleum Corporation for data acquisition. We thank the Seismic Array Laboratory, Institute of Geology and Geophysics, Chinese Academy of Sciences, Southern University of Science and Technology, Guilin University of Technology, Institute of Disaster Prevention, Prof. Zhi Zhang, Drs. Bateer Wu, Guangbing Hou, Qilin Tu, Zhiming Bai, Youshan Liu, Yuan Ling, Jincheng Xu, Minfu Huang, Weiyu Dong, Yuepeng Huang, Long Li and Yang He for their contribution during the data acquisition. We appreciate the useful suggestions from Profs. Tianyu Zheng, Laicheng Miao, Tingjie Yan, Huajian Yao, Yonghua Li, and Yong Zheng. We would like to thank two anonymous reviewers and the Editor-in-Chief for their constructive comments and suggestions to significantly improve the quality of the manuscript. This study is financially supported by the National Key Research and Development Program of China (2016YFC0600101).

Appendix A. Supplementary data

Supplementary data to this article can be found online at https://doi.org/10.1016/j.oregeorev.2022.104704.

References

Bensen, G.D., Ritzwoller, M.H., Barmin, M.P., Levshin, A.L., Lin, F., Moschetti, M.P., Shapiro, N.M., Yang, Y., 2007. Processing seismic ambient noise data to obtain reliable broad-band surface wave dispersion measurements. Geophys. J. Int. 169 (3), 1239–1260.

Boschi, L., Ekström, G., 2002. New images of the Earth's upper mantle from measurements of surface wave phase velocity anomalies. J. Geophys. Res. Solid Earth 107, ESE 1–ESE -12.

Brocher, T.M., 2005. Empirical relations between elastic wavespeeds and density in the Earth's crust. Bull. Seismol. Soc. Am. 95 (6), 2081–2092.

Deng, J., Yang, L.-Q., Groves, D.I., Zhang, L., Qiu, K.-F., Wang, Q.-F., 2020. An integrated mineral system model for the gold deposits of the giant Jiaodong province, eastern China. Earth-Sci. Rev. 208, 103274. https://doi.org/10.1016/j.earscirev.2020.103274.

Du, P., Wu, J., Li, Y., Wang, J., Han, C., Lindsay, M.D., Yuan, H., Zhao, L., Xiao, W., 2020. Imaging karatungk Cu-Ni mine in Xinjiang, Western China with a passive seismic array. Minerals 10 (7), 601. https://doi.org/10.3390/min10070601.

Du, Q., Xing, B.S., Ye, J., Yu, C.M., 2018. Application of the continuous conductivity observation system to prediction of deep prospecting in the Wulong gold deposit. Geol. Explor. 54, 332-343 (in Chinese with English abstract). https://doi.org/10.13712/j.cnki.dzykt.2018.02.011.

Duan, X., Zeng, Q., Yang, J., Liu, J., Wang, Y., Zhou, L., 2014. Geochronology, geochemistry and Hf isotope of Late Triassic magmatic rocks of Qingchengzi district in Liaodong peninsula, Northeast China. J. Asian Earth Sci. 91, 107–124.

Fang, H.J., Yao, H.J., Zhang, H.J., Huang, Y.C., van der Hilst, R.D., 2015. Direct inversion of surface wave dispersion for three-dimensional shallow crustal structure based on ray tracing: methodology and application. Geophys. J. Int. 201, 1251-1263.

Fang, W., Dai, L.-Q., Zheng, Y.-F., Zhao, Z.-F., Ma, L.-T., 2020. Tectonic transition from oceanic subduction to continental collision: New geochemical evidence from Early-Middle Triassic mafic igneous rocks in southern Liaodong Peninsula, east-central China. Geol. Soc. Am. Bull. 132 (7-8), 1469–1488.

Feng, H., Shen, P., Zhu, R., Li, C., Ma, G.e., Pan, H., 2019. Geology and He-Ar-S-Pb isotope constraints on the genesis of the Sidaogou gold deposit in Liaodong Peninsula, northeastern North China Craton. Ore Geol. Rev. 113, 103080. https://doi.org/10.1016/j.oregeorev.2019.103080.

Feng, H., Shen, P., Zhu, R., Ma, G.e., Li, C., Li, J., 2020. SIMS U-Pb dating of vein-hosted hydrothermal rutile and carbon isotope of fluids in the Wulong lode gold deposit, NE China: Linking gold mineralization with craton destruction. Ore Geol. Rev. 127, 103838. https://doi.org/10.1016/j.oregeorev.2020.103838.

Gao, B.S., Dong, Y.S., Li, F.Q., Wang, P.S., Gan, Y.C., Chen, M.S., Tian, Z.H., 2017. Petrogenesis of the Lieryu Formation of the South Liaohe Group in the Huanghuadian area. Liaodong Peninsula. Acta Petrol. Sin. 33, 2725–2742 in Chinese with English abstract.

Goldfarb, R.J., Phillips, G.N., Nokleberg, W.J., 1998. Tectonic setting of synorogenic gold deposits of the Pacific Rim. Ore Geol. Rev. 13 (1-5), 185–218.

Groves, D.I., Goldfarb, R.J., Gebre-Mariam, M., Hagemann, S.G., Robert, F., 1998. Orogenic gold deposits: a proposed classification in the context of their crustal distribution and relationship to other gold deposit types. Ore Geol. Rev. 13 (1-5), 7–27.

Gu, Y.C., Chen, R.Y., Li, D.T., Yang, J.L., Yang, F.C., Jia, H.X., Dick, J., Hu, Q.H., Ju, N., Cao, J., 2018. Jurassic ca. 160 Ma crustal remelting and Paleoproterozoic intrusive rock residues in the Liaodong Peninsula, East China: Evidence from in situ zircon U-Pb dating and Lu–Hf isotopic analysis. Geol. J. 53, 174–188.

Gu, Y.C., Zhao, Y., Yang, Z.Z., Zhang, P., Yang, F.C., Ju, N., Xu, J., Yang, H.Z., Bi, Z.W., Wei, Y.M., 2020. Zircon U-Pb ages, elements geochemistry and Sr-Nd-Pb-Hf Isotopic characteristics of Wulong remelting granite intrusive rocks in Liaodong Peninsula and geological significance. Earth Sci. J. China Univ. Geosci. 45, 3913–3933 in Chinese with English abstract.

Huang, Y.-C., Yao, H., Huang, B.-S., van der Hilst, R.D., Wen, K.-L., Huang, W.-G., Chen, C.-H., 2010. Phase velocity variation at periods of 0.5–3 seconds in the Taipei Basin of Taiwan from correlation of ambient seismic noise. Bull. Seismol. Soc. Am. 100 (5A), 2250–2263.

Li, C., Yao, H., Fang, H., Huang, X., Wan, K., Zhang, H., Wang, K., 2016. 3D near-surface shear-wave velocity structure from ambient-noise tomography and borehole data in the Hefei urban area. China. Seismol. Res. Lett. 87 (4), 882–892.

Li, L., Santosh, M., Li, S.-R., 2015a. The 'Jiaodong type'gold deposits: characteristics, origin and prospecting. Ore Geol. Rev. 65, 589–611.

Li, J., Cai, W.-Y., Wang, K.-Y., Kim, N., Liu, H.-L., Lee, G.-J., Yoo, B.-C., Liu, Y., 2020. Initial decratonization of the eastern North China Craton: New constraints from geochronology, geochemistry, and Hf isotopic compositions of Mesozoic igneous rocks in the Qingchengzi district. Geol. J. 55 (5), 3796–3820.

Li, Y.G., Zhai, M.G., Yang, J.H., Miao, L.C., Guan, H., 2004. Gold mineralization age of the Anjiayingzi gold deposit in Chifeng County, Inner Mongolia and implications for Mesozoic metallogenic explosion in North China. Sci. China, Ser. D Earth Sci. 47, 115–121.

Li, Z., Chen, B., Liu, J.W., Zhang, L., Yang, C., Chuan, Y., 2015b. Zircon U-Pb ages and their implications for the South Liaohe Group in the Liaodong Peninsula, Northeast China. Acta Petrol. Sin. 31, 1589–1605 in Chinese with English abstract.

Lin, F.-C., Ritzwoller, M.H., Snieder, R., 2009. Eikonal tomography: surface wave tomography by phase front tracking across a regional broad-band seismic array. Geophys. J. Int. 177 (3), 1091–1110.

Lin, F.-C., Li, D., Clayton, R.W., Hollis, D., 2013. High-resolution 3D shallow crustal structure in Long Beach, California: Application of ambient noise tomography on a dense seismic array. Geophysics 78 (4), Q45–Q56.

Liu, D.Y., Nutman, A.P., Compston, W., Wu, J.S., Shen, Q.H., 1992. Remnants of$\geq$ 3800 Ma crust in the Chinese part of the Sino-Korean craton. Geology 20 (4), 339. https://doi.org/10.1130/0091-7613(1992)020<0339:ROMCIT>2.3.CO;2.

Liu, J., Wang, S.L., Li, T.G., Yang, Y., Liu, F.X., Li, S.H., Duan, C., 2018. Geochronology and isotopic geochemical characteristics of Wulong gold deposit in Liaoning Province. Miner. Depos. 37, 712–728 in Chinese with English abstract.

Liu, J., Zhao, G., Xu, G., Sha, D., Xiao, C., Fang, X., Liu, F., Guo, Q.i., Yu, H., 2020a. Structural control and genesis of gold deposits in the Liaodong Peninsula, northeastern North China Craton. Ore Geol. Rev. 125, 103672. https://doi.org/10.1016/j.oregeorev.2020.103672.

Liu, X.C., Xiao, C.H., Zhang, S.H., Hu, G.H., Li, J.F., Wang, C.G., 2020b. Whether the sanguliu granite provided the energy required for forming the wulong gold deposit, liaoning province, china? J. Earth Sci. 45, 3998–4013 in Chinese with English abstract.

Luo, Y., Sun, M., Zhao, G., Li, S., Xu, P., Ye, K., Xia, X., 2004. LA-ICP-MS U-Pb zircon ages of the Liaohe Group in the Eastern Block of the North China Craton: constraints on the evolution of the Jiao-Liao-Ji Belt. Precambr. Res. 134 (3-4), 349–371.

Mao, J.W., Xie, G.Q., Li, X.F., Zhang, C.Q., Wang, Y.T., 2006. Mesozoic large-scale mineralization and multiple lithospheric extensions in South China. Acta Geol. Sin. - Engl. 80, 420-431.

Miao, L., Qiu, Y., Fan, W., Zhang, F., Zhai, M., 2005. Geology, geochronology, and tectonic setting of the Jiapigou gold deposits, southern Jilin Province. China. Ore Geol. Rev. 26 (1-2), 137–165.

Mordret, A., Roux, P., Boué, P., Ben-Zion, Y., 2019. Shallow three-dimensional structure of the San Jacinto fault zone revealed from ambient noise imaging with a dense seismic array. Geophys. J. Int. 216, 896-905.

Paige, C.C., Saunders, M.A., 1982. LSQR: An algorithm for sparse linear equations and sparse least squares. ACM Trans. Math. Software 8 (1), 43–71.

Quan, Y.-K., Yang, D.-B., Mu, M.-S., Hao, L.-R., Yang, H.-T., Wang, A.-Q., Xu, W.-L., 2020. Tectonic evolution of the northeastern North China Craton: Constraints from geochronology and Sr–Nd–Hf–O isotopic data from Late Triassic intrusive rocks on Liaodong Peninsula. NE China. Lithos 362-363, 105489. https://doi.org/10.1016/j.lithos.2020.105489.

Rawlinson, N., Sambridge, M., 2004. Wave front evolution in strongly heterogeneous layered media using the fast marching method. Geophys. J. Int. 156 (3), 631–647.

Roux, P., Moreau, L., Lecointre, A., Hillers, G., Campillo, M., Ben-Zion, Y., Zigone, D., Vernon, F., 2016. A methodological approach towards high-resolution surface wave imaging of the San Jacinto Fault Zone using ambient-noise recordings at a spatially dense array. Geophys. J. Int. 206, 980-992.

Sabra, K.G., Gerstoft, P., Roux, P., Kuperman, W.A., Fehler, M.C., 2005. Extracting time-domain Green's function estimates from ambient seismic noise. Geophys. Res. Lett. 32.

Shapiro, N.M., Campillo, M., Stehly, L., Ritzwoller, M.H., 2005. High-resolution surface-wave tomography from ambient seismic noise. Science 307 (5715), 1615–1618.

Shearer, P.M. (Ed.), 2019. Introduction to Seismology. Cambridge University Press.

Sun, J.-F., Zhang, J.-H., Yang, J.-H., Zhu, Y.-S., Chen, J.-Y., Ling-Hu, M.-M., 2021. Multi-stage Jurassic magmatism in the Liaodong Peninsula: Constraints on crustal evolution beneath the eastern North China Craton. Lithos 402-403, 105897. https://doi.org/10.1016/j.lithos.2020.105897.

Wang, G.C., Tian, X.B., Guo, L.L., Yan, J.Y., Lyu, Q.T., 2018a. High-resolution crustal velocity imaging using ambient noise recordings from a high-density seismic array: An example from the Shangrao section of the Xinjiang basin. China. Earthq. Sci. 31, 242–251.

Wang, Y., Wang, F., Wu, L., Shi, W., Yang, L., 2018b. (U-Th)/He thermochronology of metallic ore deposits in the Liaodong Peninsula: Implications for orefield evolution in northeast China. Ore Geol. Rev. 92, 348–365.

Wang, Y., Yu, B., Zeng, Q., Guo, W., Yang, J., Meng, Q., 2019. Petrogenesis and tectonic setting of the Wulong two-mica monzogranite on Liaodong Peninsula, NE China: Constraints from zircon U-Pb and Hf-O isotopic data. Geol. J. 53 (4), 261–279.

Wang, Z.Q., Hu, H.Z.F., Chen, B., Duan, X.X., Zhou, T.F., Jiang, X., 2020. The petrogenesis of the Early Cretaceous Sanguliu pluton in the Liaodong Peninsula, NE China: Constrained from the trace-element modelling and Sr-Nd isotopes. Acta Petrol. Sin. 36, 3683–3704 in Chinese with English abstract.

Wen, B.-J., Fan, H.-R., Santosh, M., Hu, F.-F., Pirajno, F., Yang, K.-F., 2015. Genesis of two different types of gold mineralization in the linglong gold field, China: constrains from geology, fluid inclusions and stable isotope. Ore Geol. Rev. 65, 643–658.

Wu, F., Lin, J., Wilde, S., Zhang, X., Yang, J., 2005. Nature and significance of the Early Cretaceous giant igneous event in eastern China. Earth Planet. Sci. Lett. 233 (1-2), 103–119.

Wu, F.-Y., Yang, J.-H., Xu, Y.-G., Wilde, S.A., Walker, R.J., 2019. Destruction of the North China craton in the Mesozoic. Annu. Rev. Earth Planet. Sci. 47 (1), 173–195.

Xiao, W., Windley, B.F., Hao, J., Zhai, M., 2003. Accretion leading to collision and the Permian Solonker suture, Inner Mongolia, China: Termination of the central Asian orogenic belt. Tectonics 22 (6), n/a–n/a.

Yang, J.-H., Sun, J.-F., Chen, F., Wilde, S.A., Wu, F.-Y., 2007a. Sources and petrogenesis of Late Triassic dolerite dikes in the Liaodong Peninsula: implications for post-collisional lithosphere thinning of the eastern North China Craton. J. Petrol. 48 (10), 1973–1997.

Yang, J.-H., Sun, J.-F., Zhang, J.-H., Wilde, S.A., 2012. Petrogenesis of Late Triassic intrusive rocks in the northern Liaodong Peninsula related to decratonization of the North China Craton: Zircon U-Pb age and Hf–O isotope evidence. Lithos 153, 108–128.

Yang, J.-H., Wu, F.-Y., Wilde, S.A., Belousova, E., Griffin, W.L., 2008a. Mesozoic decratonization of the North China block. Geology 36 (6), 467. https://doi.org/10.1130/G24518A.110.1130/2008113.

Yang, Y., Li, A., Ritzwoller, M.H., 2008b. Crustal and uppermost mantle structure in southern Africa revealed from ambient noise and teleseismic tomography. Geophys. J. Int. 174 (1), 235–248.

Yang, Y., Ritzwoller, M.H., Levshin, A.L., Shapiro, N.M., 2007b. Ambient noise Rayleigh wave tomography across Europe. Geophys. J. Int. 168 (1), 259–274.

Yang, Y., Shen, W., Ritzwoller, M.H., 2011. Surface wave tomography on a large-scale seismic array combining ambient noise and teleseismic earthquake data. Earthq. Sci. 24 (1), 55–64.

Yang, Y., Zheng, Y., Chen, J., Zhou, S., Celyan, S., Sandvol, E., Tilmann, F., Priestley, K., Hearn, T.M., Ni, J.F., Brown, L.D., Ritzwoller, M.H., 2010. Rayleigh wave phase velocity maps of Tibet and the surrounding regions from ambient seismic noise tomography. Geochem. Geophys. Geosyst. 11 (8), n/a–n/a.

Yao, H., van der Hilst, R.D., de Hoop, M.V., 2006. Surface-wave array tomography in SE Tibet from ambient seismic noise and two-station analysis—I. Phase velocity maps. Geophys. J. Int. 166 (2), 732–744.

Yu, B., Zeng, Q., Frimmel, H.E., Wang, Y., Guo, W., Sun, G., Zhou, T., Li, J., 2018. Genesis of the Wulong gold deposit, northeastern North China Craton: Constraints from fluid inclusions, HOS-Pb isotopes, and pyrite trace element concentrations. Ore Geol. Rev. 102, 313–337.

Yu, B., Zeng, Q.D., Frimmel, H.E., Qiu, H.C., Li, Q.L., Yang, J.H., Wang, Y.B., Zhou, L.L., Chen, P.W., Li, J.P., 2020a. The 127 Ma gold mineralization in the Wulong deposit, Liaodong Peninsula, China: constraints from molybdenite re-Os, monazite U-Th-Pb, and zircon U-Pb geochronology. Ore Geol. Rev. 121, 103542.

Yu, B., Zeng, Q.D., Xia, F., Qiu, H.C., Li, J.P., Xie, L.Q., Chen, X.Y., Yu, B.S., 2020b. Structural superimposed halo of the Wulong gold deposit in Liaoning Province. Geol. Explor. 56, 0898–914 in Chinese with English abstract.

Yu, G., Xu, T., Ai, Y., Chen, L., Yang, J., 2020c. Significance of crustal extension and magmatism to gold deposits beneath Jiaodong Peninsula, eastern North China Craton: Seismic evidence from receiver function imaging with a dense array. Tectonophysics 789, 228532. https://doi.org/10.1016/j.tecto.2020.228532.

Zeng, Q.D., Chen, R.Y., Yang, J.H., Sun, G.T., Yu, B., Wang, Y.B., Chen, P.W., 2019. The metallogenic characteristics and exploring ore potential of the gold deposits in eastern Liaoning Province. Acta Petrol. Sin. 35, 1939–1963 in Chinese with English abstract.

Zhai, M., Yang, J., Fan, H., Miao, L., Li, Y., 2002. A large-scale cluster of gold deposits and metallogenesis in the eastern North China Craton. Int. Geol. Rev. 44 (5), 458–476.

Zhai, M.G., Zhu, R.X., Liu, J.M., Meng, Q.R., Hou, Q.L., Hu, S.B., Liu, W., Li, Z., Zhang, H. F., Zhang, H.F., 2004. Time range of Mesozoic tectonic regime inversion in eastern North China Block. Sci. China, Ser. D Earth Sci. 47, 151–159 in Chinese with English abstract.

Zhang, P., Zhao, Y., Chai, P., Yang, H.-Z., Na, F.-C., 2017. Geochemistry, Zircon U-Pb analysis, and biotite 40Ar/39Ar geochronology of the Maoling gold deposit, Liaodong rift, NE China. Resour. Geol. 67 (4), 426–441.

Zhang, P., Kou, L.-L., Zhao, Y., Bi, Z.-W., Sha, D.-M., Li, Z.-M., Han, R.-P., 2019a. Fluid inclusions, HO, S, Pb, and noble gas isotope studies of the Baiyun gold deposit in the Qingchengzi orefield, NE China. J. Geochem. Explor. 200, 37–53.

Zhang, S., Zhu, G., Xiao, S., Su, N., Liu, C., Wu, X., Yin, H., Li, Y., Lu, Y., 2020. Temporal variations in the dynamic evolution of an overriding plate: Evidence from the Wulong area in the eastern North China Craton, China. Geol. Soc. Am. Bull. 132 (9-10), 2023–2042.

Zhang, Z., Wang, G., Carranza, E.J.M., Zhang, J., Tao, G., Zeng, Q., Sha, D., Li, D., Shen, J., Pang, Z., 2019b. Metallogenic model of the Wulong gold district, China, and associated assessment of exploration criteria based on multi-scale geoscience datasets. Ore Geol. Rev. 114, 103138. https://doi.org/10.1016/j.oregeorev.2019.103138.

Zhu, R., Fan, H., Li, J., Meng, Q., Li, S., Zeng, Q., 2015. Decratonic gold deposits. Sci. China Earth Sci. 58 (9), 1523–1537.